Supporting Information

Photocatalytic Conversion of Methane to Ethane and Propane Using Cobalt-Cluster-Activated GaN Nanowires

Zhengwei Ye[a]†, Zhuoran Long[b]†, Bingxing Zhang[a]*, Ishtiaque Ahmed Navid[a], Jan Paul Menzel[b], Yifan Shen[a], Shubham Mondal[a], Facheng Guo[b], Theodore B. Norris[a]*, Victor S. Batista[b]*, Zetian Mi[a]*

[a] Z. W. Ye, B. X. Zhang, I. A. Navid, Y. F. Shen, S. Mondal, Prof. T. B. Norris, Prof. Z. Mi

Department of Electrical Engineering and Computer Science

University of Michigan, Ann Arbor

1301 Beal Avenue, Ann Arbor, MI 48109, USA

E-mail: bingxinz@umich.edu; tnorris@umich.edu; ztmi@umich.edu

[b] Z. R. Long, J. P. Menzel. F. C. Guo, Prof. V. S. Batista

Department of Chemistry

Yale University

2225 Prospect Street, New Haven, CT 06520, USA

E-mail: victor.batista@yale.edu

†These authors contribute equally.

List of content

1. Materials and methods

Synthesis of *p*-type GaN nanowires. 3-inch *p*-type GaN nanowires wafer were synthesized using PAMBE (Plasma-Assisted Molecular Beam Epitaxy) technology on silicon substrate [1]. The substrate underwent a thorough cleaning process involving acetone, methanol and 10% buffered hydrofluoric acid soaking. Together with an in-situ annealing procedure carried out at approximately 850°C within the reaction chamber, most remaining oxide on the silicon wafer was eliminated, just before the growth phase. The growth of GaN nanowires (NWs) was initiated spontaneously on the silicon wafer under nitrogen-rich conditions. This growth process involved a precise control of Ga and Mg fluxes through the use of thermal effusion cells, coupled with nitrogen radicals, which are essential for the growth, generated from a radio-frequency nitrogen plasma source.

Cocatalyst loading. The Co clusters were deposited onto GaN nanowires through a standard photoreduction process. In a sequential procedure, a photocatalyst wafer (0.8 cm by 0.8 cm) was secured on a Teflon holder, placed at the bottom of a 390 mL Pyrex chamber containing 50 mL of a 20% methanol aqueous solution. Subsequently, 10 μL of a 0.2 mol L^{-1} $CoCl_2$ solution (Sigma-Aldrich) was added to the chamber. The chamber, equipped with a quartz lid and a vacuum-tight O-ring, was evacuated before the photoreduction process. Following evacuation, the chamber underwent 30 minutes of irradiation using a 300 W Xenon lamp (Cermax, PE300BUV). Finally, the photocatalyst wafer was rinsed with deionized water and dried at 80°C under a vacuum atmosphere.

2. Characterization

The X-ray diffraction (XRD) pattern of photocatalyst wafer was obtained by a Rigaku X-ray diffractometer equipped with Cu Kα radiation working at the accelerating voltage of 40 kV, the current of 80 mA and the scanning rate of 0.05° 2θ s^{-1}. The microcosmic morphology of samples was examined by a TESCAN MIRA3 field emission scanning electron microscopy (FESEM) at an acceleration voltage of 10 kV. The atomic-scale structures of as-prepared samples were analyzed on a spherical aberration corrected scanning transmission electron microscopy (Thermo Fisher Spectra 300 Probe-Corrected S/TEM) with a 300 kV accelerating voltage which generated the high-resolution transmission electron microscopy (HRSTEM) and high-angle annular dark field scanning transmission electron microscopy (HAADF-STEM) images. In the TRPL measurement, the samples were excited with the 365 nm output with 12.5 bandwidth from the second harmonic of a 78 MHz/100 fs Ti:sapphire laser, focused to a spot of 50 μm diameter. The photoluminescence transient was taken by a streak camera system with a time resolution of 2 ps and a spectral resolution of 0.14 nm.

3. Catalytic performance measurement

Photocatalytic non-oxidation methane coupling. Photocatalytic non-oxidative methane coupling was conducted in a 400 mL Pyrex chamber under a 300W Xenon lamp. The photocatalyst wafer, with a prepared area of 0.64 cm^2, was positioned at the bottom of the reaction chamber and immersed in 20 mL of deionized water. The

concentrated light intensity on the photocatalyst wafer was measured at 6 W cm^{-2} using a thermopile detector (919P, Newport Corporation). Subsequently, methane feed gas was introduced into the chamber at atmospheric pressure. Gas samples from the chamber were manually collected every hour (1.5 hours in the stability test) using a syringe and analyzed in a gas chromatograph (Shimadzu GC-2010) FID detector.

The reaction formula for ethane generation: $2CH_4 \rightarrow C_2H_6 + H_2$ (1)

The reaction formula for propane generation: $3CH_4 \rightarrow C_3H_8 + 2H_2$ (2)

The mass density of GaN was 6.1 g cm^{-3}. The amount of photocatalyst on silicon wafer used in the photocatalytic methane reforming was calculated to be ~4.7 μmol cm^{-2} (or ~0.39 mg cm^{-2}). The amount of co-catalysts on GaN nanowires was examined through ICP test to be ~0.5 μg cm^{-2} (**Table S1**).

4. Density function theory calculation

Theoretical Simulation. Density functional theory calculations are performed utilizing Vienna Ab Initio Simulation Package (VASP) 5.4.1 package [2] with the Perdew-Berke-Ernzerhof (PBE) exchange correlation functional [3]. The projector-augmented wave (PAW) method [2e, 4] is used with a 450 eV cutoff and the Gaussian smearing (σ = 0.1). The electron structure convergence criterion is 10^{-5} eV and the geometry optimization criterion is 10^{-4} eV. Grimme's DFT-D3 dispersion correction is applied with Becke-Johnson damping [5]. Calculations without the dispersion correction are also performed for the methane activation steps to compare with previous results. All geometries shown in Figure 3, 4, S1 and S2 are visualized using the VESTA program [6].

For the Co system, the bulk geometry optimization is performed on a supercell consisting of 3*3*1 Co hcp unit cells (18 Co atoms in total) with an 11*11*21 Monkhorst-Pack (MP) k-point grid centered at the Γ point. The first order Methfessel-Paxton smearing (σ = 0.1) [7] is used for this bulk geometry optimization instead of Gaussian smearing. Different magnetizations are tested and the system with 28 more electrons in the alpha channel (spin-up) than the beta channel (spin-down) gives the lowest energy. The result hexagonal unit cell vectors are a = b = 2.465 Å and c = 3.981 Å. Similar calculations employing Gaussian smearing also gives the same minimum-energy magnetization and a very close bulk geometry (smaller than 0.001 Å differences of cell vectors). The Co slab is constructed based on the optimized bulk geometry by doubling the system size, which contains 3*3 Co atoms per layer and 4 layers along the [0001] surface (36 Co atoms in total), and the hexagonal box has a = b = 7.396 Å and c = 35 Å. For all Co slab systems, the bottom two layers are frozen and the top two layers are relaxed during the geometry optimization with a 5*5*1 MP k-point grid centered at the Γ point and different magnetizations. The minimum-energy magnetization is 61 for the Co slab, and all energies and energy changes in **Figure 3** are calculated from corresponding minimum-energy magnetization states.

For the GaN system, the bulk geometry optimization is performed on the hexagonal unit cell containing two Ga atoms and two N atoms, with a 21*21*21 MP k-point grid centered at the Γ point and an increased 600 eV plane wave basis cutoff. The result cell vectors are a = b = 3.196 Å and c = 5.210 Å. The slab is constructed along the

$[1\bar{1}00]$ surface based on the optimized geometry, consisting of 4 layers with 2*4 unit cells per layer (64 Ga and 64 N atoms in total). The result box size is 10.423*12.783*32 $Å^3$. For all GaN slab systems, the bottom 3 layers are frozen, and the top layer is relaxed for the geometry optimization with a 3*3*1 MP k-point grid centered at the Γ point.

For the cluster model (Co_7-GaN) used for density of states (DOS) calculations, a GaN slab of 3*4*4 is used. A monolayer cluster of 7 Co atoms are placed on the GaN surface and the rest of GaN surface are covered by dissociated water (Ga*-OH and N*-H). The bottom 3 GaN layers are kept frozen while all the other atoms are relaxed during the geometry optimization at the Γ point. A total magnetization of 15 gives the minimum energy. With the optimized geometry, a single point calculation is performed with a 3*3*1 MP k-point grid centered at the Γ point. The projected density of states for each elements are extracted using the VASPKIT package [8].

Table S1. AES-ICP measurement on varied precursor dosage.

Sample Id	Co 59 (ppb)	ug/cm^2	wt(%)
0.5 µl (0.2 M $CoCl_2$)	0.016	0.0390	0.0099
2 µl (0.2 M $CoCl_2$)	0.082	0.2038	0.0516
5 µl (0.2 M $CoCl_2$	0.203	0.5077	0.1284
10 µl (0.2 M $CoCl_2$)	0.553	1.382	0.3486
20 µl (0.2 M $CoCl_2$)	0.770	1.926	0.4852
50 µl (0.2 M $CoCl_2$)	1.609	4.022	1.0080

Table S2. State-of-the-art photocatalytic systems for non-oxidation coupling of methane.

Photocatalysts	Condition	C products Rate ($\mu mol\ h^{-1}$)	C_2 selectivity	Stability (hours)	Year [Ref.]
$Co_{0.1}$/p-GaN	300W Xe lamp, irradiance range from 0.1 to 6 W cm^{-2}; CH_4 = 0.1 MPa	Ethane: 192307; Propane: 17948	91.4	111	This work
Pd-[8]TiO_2	300W Xe lamp, 50ml H_2O, CH_4 (99.999%)	326 (methane conversion rate)	81	24	2024[9]
Au C-ZnO	300W Xe lamp, irradiance 100 mW cm^{-2}; 1.5 vol% CH_4/Ar	45 (ethane)	96.04	12	2023[10]
$[Fe(H_2O)_5OH]^{2+}$ complex	Multi wavelength LED irradiation ,100% CH_4	8.4 (ethane)	94	2	2023[11]
Au-Pd Bi_2NbO_5F	300W Xe Lamp, irradiance 500mW cm^{-2}, 1ml/170ml CH_4/Ar	22.6 (ethylene)	63	4	2023[12]
Pt-Black TiO_2	300W Xe lamp, λ > 400nm, 100 μmol CH_4	41 (propane)	65	80	2022[13]
ZnO GaN SS-F	300W Xe Lamp, 300 μmol pure CH_4	330 (methane conversion rate)	98	70	2021[14]
Ag-HPW TiO_2	400W Xe lamp (Newport), 0.1 g samples; CH_4 = 0.3 MPa	4.9 (ethane)	90	72.5	2020[15]
Ga^{3+} ETS-10	150 W high-pressure Hg lamp for 5 h; 0.2 g sample; 200 μmol CH_4	5.69 (ethane)	~100	5	2012[16]
Zn^{+}-modified ZSM-5 zeolite	150 W high-pressure Hg lamp for 8 h; 1 g sample; 200 μmol CH_4	9.8 (ethane)	99	8	2011[17]

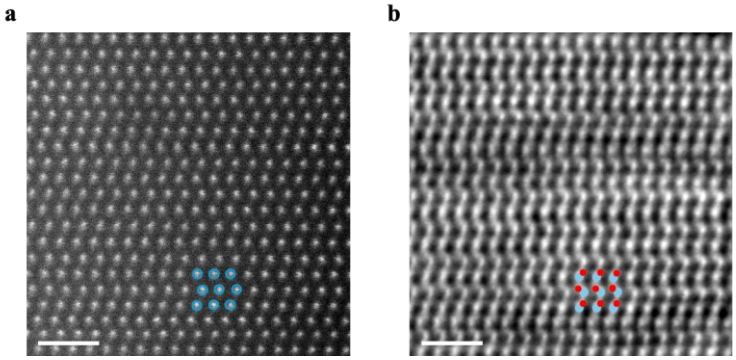

Figure S1. (a) HAADF and (b) iDPC STEM images of p-GaN side wall (m-plane). The blue circles and balls indicate Ga atom. The red balls indicate N atom. The scale bar indicates 1 nm.

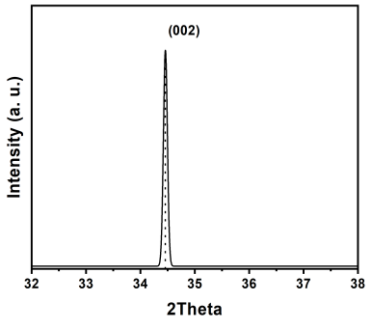

Figure S2. XRD pattern of $Co_{0.1}$/p-GaN.

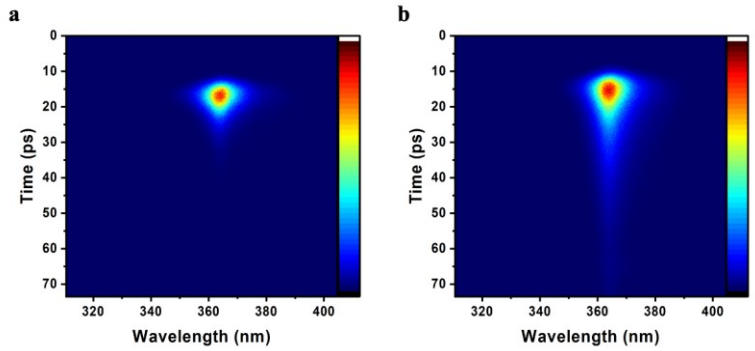

Figure S3. Streak camera plot of time resolved photoluminescence spectra of (a) p-GaN, (b) Co/p-GaN NWs device.

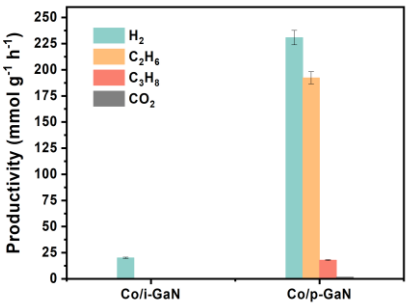

Figure S4. PNOCM performance between cobalt cluster loaded intrinsic GaN nanowires and Mg doped p-type GaN nanowires.

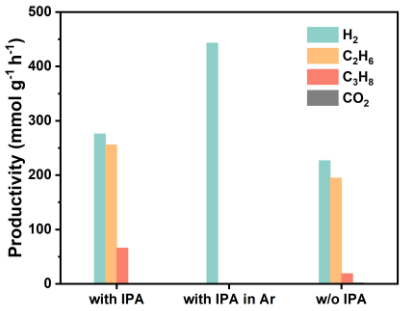

Figure S5. PNOCM performance with or without existence of hydroxyl radical scavenger (IPA).

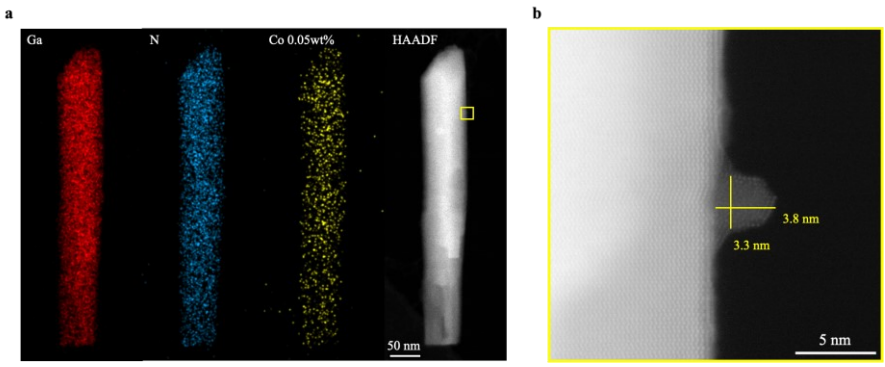

Figure S6. (a) HAADF and EDS mapping STEM image of one GaN nanowire with 0.05 wt% cobalt loaded. (b) High resolution HAADF image of GaN surface with 0.05 wt% cobalt loading.

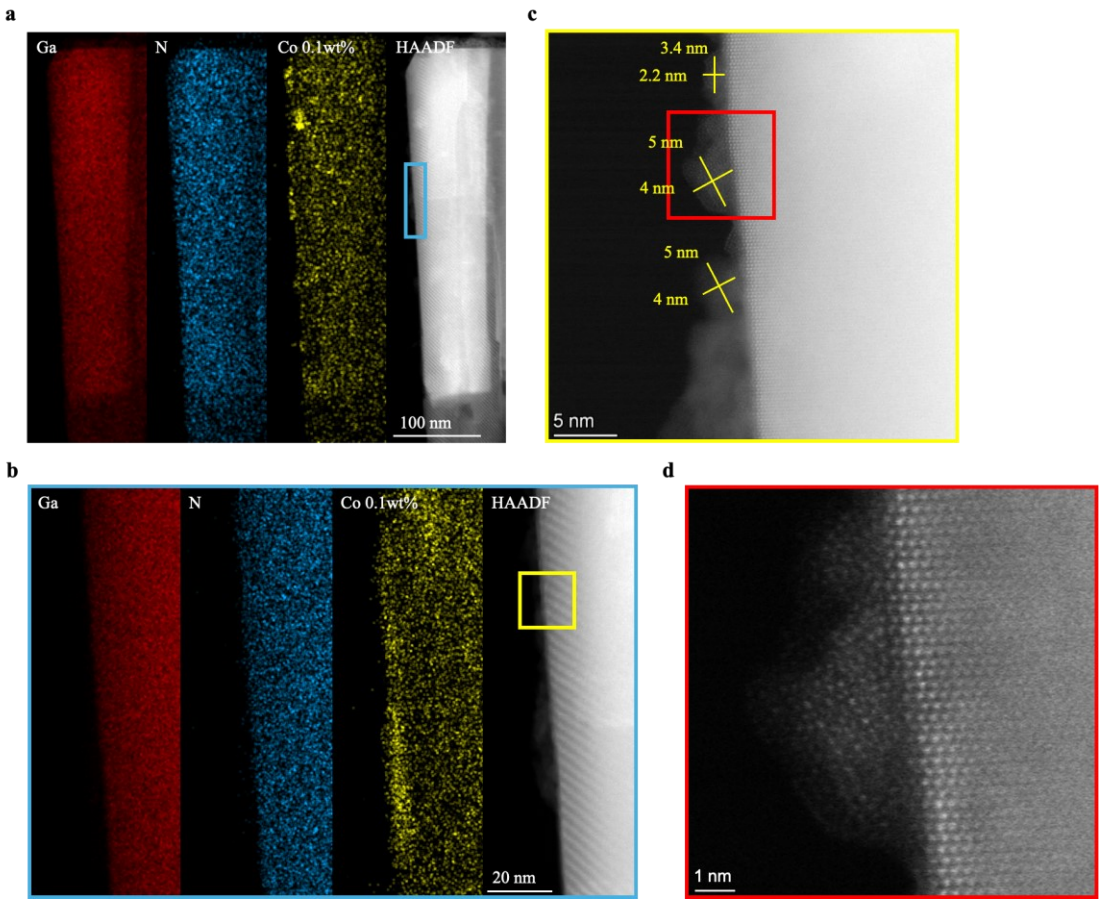

Figure S7. (a), (b) HAADF and EDS mapping STEM image of one GaN nanowire with 0.1 wt% cobalt loaded. (c), (d) High resolution HAADF image of 0.1 wt% cobalt loaded GaN surface.

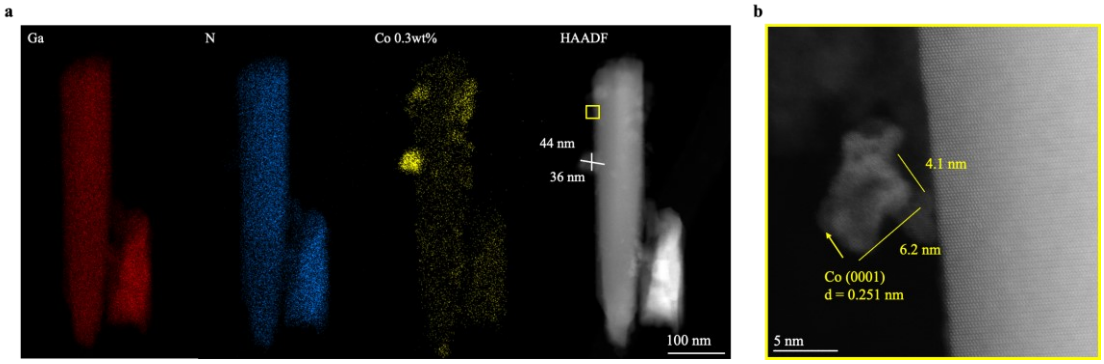

Figure S8. (a) HAADF and EDS mapping STEM image of one GaN nanowire with 0.3 wt% cobalt loaded. (b) High resolution HAADF image of 0.3 wt% cobalt loaded GaN surface.

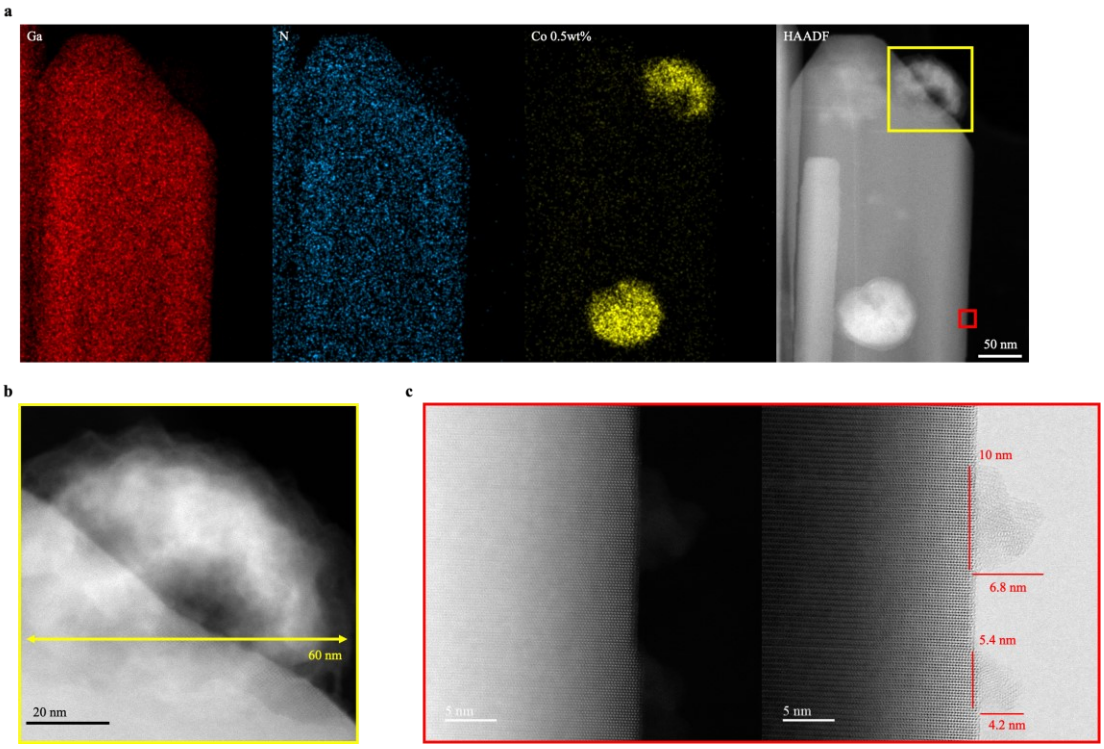

Figure S9. (a) HAADF and EDS mapping STEM image of one GaN nanowire with 0.5 wt% cobalt loaded. (b) HAADF image of 0.5 wt% cobalt loaded GaN surface. (c) High resolution HAADF and BF image of 0.5 wt% cobalt loaded GaN surface.

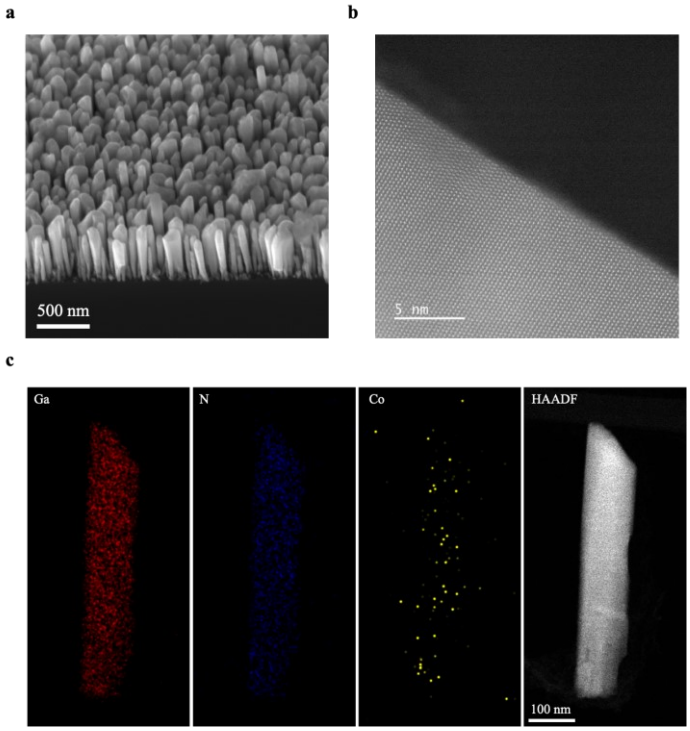

Figure S10. (a) Top, (b) 45° side view of Co/p-GaN nanowires array after 111 hours reaction. (c) HAADF STEM image of p-GaN surface after 111 hours reaction, the crystal structure is well preserved. EDS elemental mapping of Co/p-GaN nanowire after 111 hours reaction.

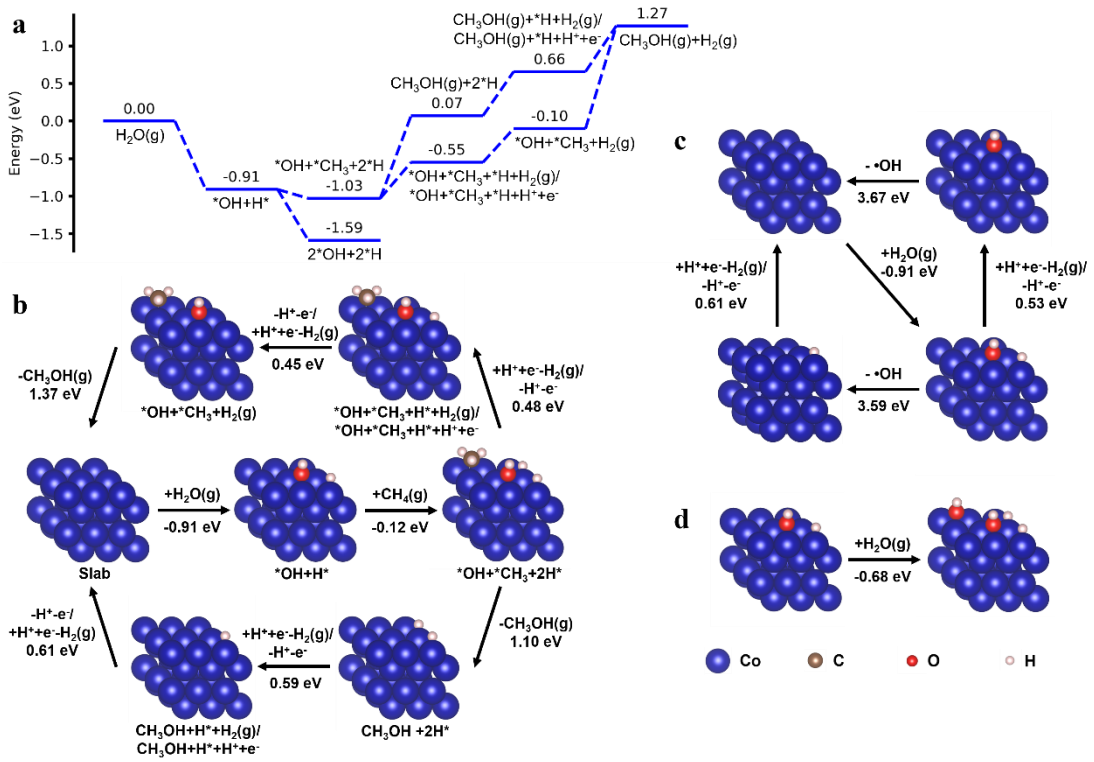

Figure S11. (a) Energy diagram and (b), (d) reaction scheme for water dissociation and methanol formation, and (c) •OH radical release. The values in (a) are system energy relative to the starting state in eV. All numbers are rounded to two decimal places. The water dissociative adsorption to the Co surface, is energetically very favorable. It is also more favorable than methane dissociative adsorption. However, the water dissociative adsorption does not lead to oxygen evolution from our experimental observations, nor any methanol production, according to our experimental observations. The latter is because of the high energy required by methanol desorption as shown in (a), (b). This also means that the opposite process, i.e., methanol dissociative adsorption, is energetically very favorable. On the other hand, forming a hydroxyl radical (•OH) is also energetically very unfavorable. The overall reaction of •OH radical formation, i.e., H_2O (g) + H^+ + e^- → •OH + H_2 (g) or H_2O (g) - H^+ - e^- → •OH, requires an energy of 3.29 eV from our calculations. On the Co surface after water dissociative adsorption, releasing the •OH requires 3.59 eV before the hydrogen evolution reaction or 3.67 eV after the hydrogen evolution reaction. Such high energy is not thermally accessible under condition of our experiments.

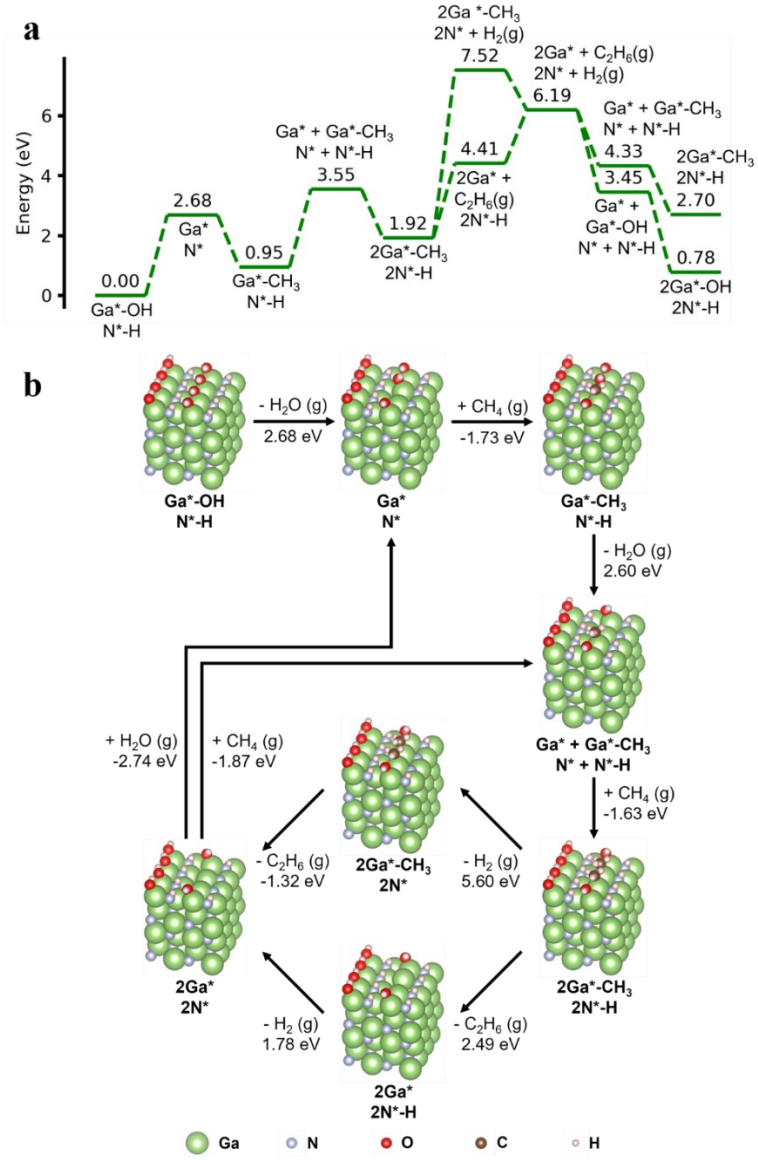

Figure S12. (a) Energy diagram and (b) reaction scheme for surface site generation, methane activation, C-C coupling and hydrogen evolution by thermal activation on the GaN nanowire surface from density function theory calculations with the slab model. The values in (a) are system energy relative to the starting state in eV. All numbers are rounded to two decimal places. Based on the analysis in the main content, this surface is covered by dissociated water (Ga*-OH and N*-H, where Ga* refers to the surface Ga atoms and N* refers to surface N atoms). Thermal generation of catalytic surface sites breaks the strong N*-H interaction, wherefore requires more energy than electrochemistry activation (see **Figure 4** in the main content), and the energy release by methane activation is not enough to compensate that. Similarly, thermal hydrogen evolution breaks two N*-H bond, which requires 5.60 eV with the presence of two neighboring Ga*-CH_3 and 1.78 eV with two neighboring empty Ga* sites. Overall, the higher energy requests make thermal activation routes less possible than electrochemistry routes.

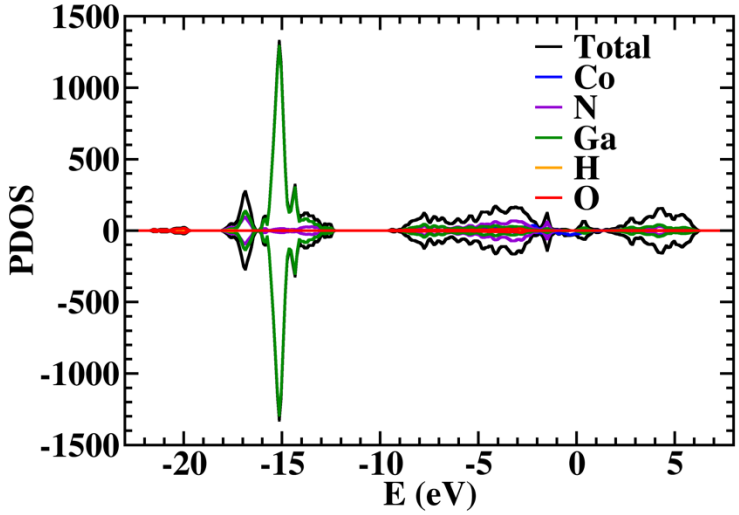

Figure S13. Total density of states (DOS) and projected density of states (PDOS) of each element for the Co_7-GaN cluster model. **Figure 5a** in the main content is the zoom-in around the GaN band gap (Fermi energy E_F = -0.69 eV). Positive density corresponds to the alpha channel and negative density corresponds to the beta channel.

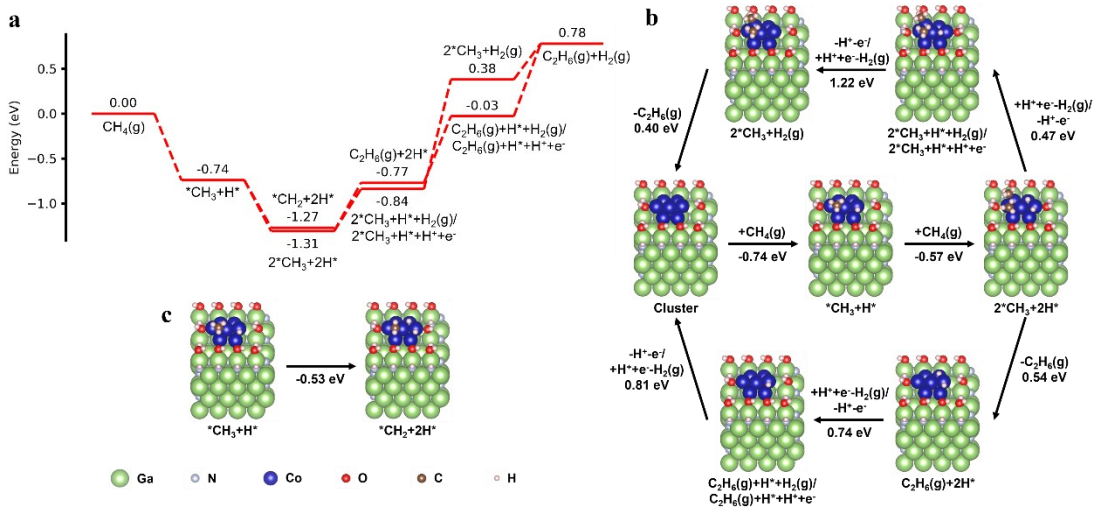

Figure S14. (a) Energy diagram and (b), (c) reaction scheme for methane reaction on the cluster model. The values in (a) are system energy relative to the starting state in eV. All numbers are rounded to two decimal places. The cluster model is the same as the one in Figure 5 of the main content. Comparing to the Co slab model, the mathene activation is energetically more favorable. This is reasonable as the Co atoms at the Co-GaN interface are less coordinated than Co atoms on the slab surface and, consequently, they are more catalytically active. Interestingly, the further activation of the methyl group to methylene is exothermic, different from the observation on the Co slab, suggesting that the Co-GaN boundary might be involved in producing the propane. After the dissociative adsorption of the second methane to the Co cluster, for the branch that hydrogen evolution reaction (HER) happens before C-C coupling and releasing the ethane, the second step of the electrochemical HER requires much more energy (and therefore, much higher potential) than Co slab due to the same reason. In the other branch that the ethane is release before the HER, the release of ethane requires 0.54 eV energy, again due to the Co-GaN interface. These observations make the Co/GaN interface less likely participate in the C-C coupling/HER reactions.

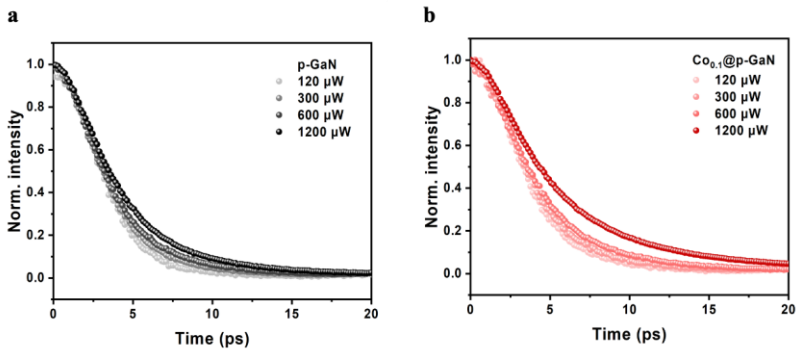

Figure S15. Excitation intensity-dependent TRPL decay curve of (a) p-GaN, (b) $Co_{0.1}$/p-GaN NWs device.

Reference

[1] a) M. G. Kibria, H. P. T. Nguyen, K. Cui, S. Zhao, D. Liu, H. Guo, M. L. Trudeau, S. Paradis, A.-R. Hakima, Z. Mi, *ACS Nano* **2013**, *7*, 7886-7893; b) M. G. Kibria, Z. Mi, *J Mater Chem A* **2016**, *4*, 2801-2820.

[2] a) G. Kresse, J. Furthmüller, *Computational Materials Science* **1996**, *6*, 15-50; b) G. Kresse, J. Furthmüller, *Physical Review B* **1996**, *54*, 11169-11186; c) G. Kresse, J. Hafner, *Physical Review B* **1993**, *47*, 558-561; d) G. Kresse, J. Hafner, *Physical Review B* **1994**, *49*, 14251-14269; e) G. Kresse, D. Joubert, *Physical Review B* **1999**, *59*, 1758-1775.

[3] J. P. Perdew, K. Burke, M. Ernzerhof, *Physical Review Letters* **1996**, *77*, 3865-3868.

[4] P. E. Blöchl, *Physical Review B* **1994**, *50*, 17953-17979.

[5] a) S. Grimme, J. Antony, S. Ehrlich, H. Krieg, *The Journal of Chemical Physics* **2010**, *132*; b) S. Grimme, S. Ehrlich, L. Goerigk, *Journal of Computational Chemistry* **2011**, *32*, 1456-1465.

[6] K. Momma, F. Izumi, *Journal of Applied Crystallography* **2011**, *44*, 1272-1276.

[7] M. Methfessel, A. T. Paxton, *Physical Review B* **1989**, *40*, 3616-3621.

[8] V. Wang, N. Xu, J.-C. Liu, G. Tang, W.-T. Geng, *Computer Physics Communications* **2021**, *267*, 108033.

[9] H. Zhang, P. Sun, X. Fei, X. Wu, Z. Huang, W. Zhong, Q. Gong, Y. Zheng, Q. Zhang, S. Xie, G. Fu, Y. Wang, *Nat. Commun.* **2024**, *15*, 4453.

[10] J. Wang, Y. Peng, W. Xiao, *Science China Chemistry* **2023**.

[11] H. Zhang, W. Zhong, Q. Gong, P. Sun, X. Fei, X. Wu, S. Xu, Q. Zhang, G. Fu, S. Xie, Y. Wang, *Angew. Chem. Int. Ed.* **2023**, *62*, e202303405.

[12] C. Tang, S. Du, H. Huang, S. Tan, J. Zhao, H. Zhang, W. Ni, X. Yue, Z. Ding, Z. Zhang, R. Yuan, W. Dai, X. Fu, M. B. J. Roeffaers, J. Long, *ACS Catalysis* **2023**, *13*, 6683-6689.

[13] L. Zhang, L. Liu, Z. Pan, R. Zhang, Z. Gao, G. Wang, K. Huang, X. Mu, F. Bai, Y. Wang, W. Zhang, Z. Cui, L. Li, *Nat. Energy* **2022**, *7*, 1042-1051.

[14] G. Wang, X. Mu, J. Li, Q. Zhan, Y. Qian, X. Mu, L. Li, *Angew. Chem. Int. Ed.* **2021**, *60*, 20760-20764.

[15] X. Yu, V. L. Zholobenko, S. Moldovan, D. Hu, D. Wu, V. V. Ordomsky, A. Y. Khodakov, *Nat. Energy* **2020**, *5*, 511-519.

[16] L. Li, Y.-Y. Cai, G.-D. Li, X.-Y. Mu, K.-X. Wang, J.-S. Chen, *Angew. Chem. Int. Ed.* **2012**, *51*, 4702-4706.

[17] L. Li, G.-D. Li, C. Yan, X.-Y. Mu, X.-L. Pan, X.-X. Zou, K.-X. Wang, J.-S. Chen, *Angew. Chem. Int. Ed.* **2011**, *50*, 8299-8303.